ACS Sustainable Chemistry & Engineering

pubs.acs.org/journal/ascecg



Research Article

# Rethinking Biochar Reinforcement Role in Elastomer Composites for Greener Tire Manufacture

C. Di Bernardo, M. Messori, and C. Noè*

Cite This: ACS Sustainable Chem. Eng. 2025, 13, 15421−15434

Read Online

ACCESS | Metrics & More | Article Recommendations | Supporting Information

**ABSTRACT:** Carbon black (CB) production in tire manufacturing has prompted the search for sustainable alternatives to address the environmental concern related to its fossil origin. Replacing fossil CB in the rubber industry is imperative for reducing the environmental footprint of vulcanized elastomer composites used in tire treads, especially in the current circular economy and decarbonization scenario. In this study, we investigate the potential use of biochar as an elastomer reinforcing agent by substituting CB in natural rubber/styrene−butadiene rubber (SBR) composites. Three varieties of biochar, derived from oilseed rape straw, miscanthus straw, and softwood pellets, were incorporated at 30, 50, and 70 phr by replacing the CB counterpart. Detailed physicochemical characterization was performed using FTIR, DLS, BET surface area analysis, and SEM to elucidate the role of morphological and structural parameters such as porosity, particle size, surface chemistry, and aromaticity in filler−matrix interaction. Mechanical and dynamic mechanical analyses suggested that biochar does not follow the classical CB reinforcement paradigm, where the surface area and particle size are dominant. Instead, reinforcement is a result of specific oxygen-containing surface functional groups in the biochar mesoporous architecture, which mediate the polymer−filler entanglement. Among the studied materials, oilseed rape straw biochar pyrolyzed at 700 °C ($OSR_{700}$) exhibited optimal dispersion, superior interfacial adhesion, and the best balance between tensile strength (3.8 MPa) and toughness (1380 MJ $m^{-3}$). In contrast, softwood-derived and lower-temperature biochar showed poor dispersion and limited reinforcement due to unfavorable pore size or excessive hydrophilicity. The research demonstrates that tailored biochar represents a promising, scalable, and environmentally sustainable alternative to carbon black in tire manufacturing. This innovation has the potential to produce high-performance tires with a significantly reduced environmental footprint. Moreover, the implications of this study extend beyond the tire industry, offering valuable insights for sustainable composites, energy dissipation materials, and green polymer engineering.

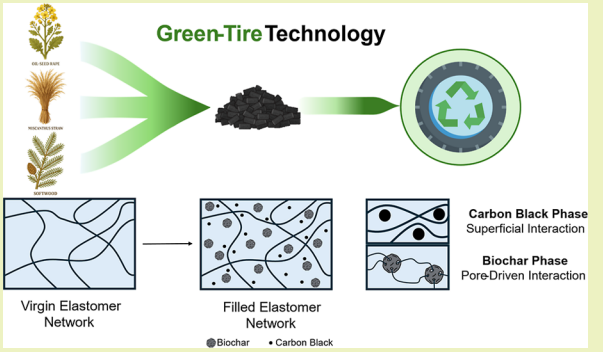


**KEYWORDS:** *biochar, tire manufacturing, rubber reinforcement, surface chemistry, filler−polymer interaction, payne effect, low carbon footprint, renewable fillers, sustainable, toughness*



## INTRODUCTION

Among the current polymer technological applications, elastomer composites are pivotal materials for tire production. Their unique mechanical properties, particularly high tensile strength and fatigue resistance, make them fundamental for automotive applications, with elastomer production rising yearly.[1,2] In 2018, tire manufacturing alone accounted for 17.1 million tons of elastomer use, with Asia as the principal producer with 67% share, followed by Europe (18%) and the US (15%) (Figure 1b). However, tire architecture is a complex assembly of metal threads with interwoven fabrics kept together by the elastomeric matrix, which complicates material recovery once discarded. The low recyclability of tires, paired with the large production volume, poses a significant environmental problem due to poor end-of-life management of discarded tires, with 48% of tires produced being landfilled or incinerated. Additionally, tire production strictly depends on carbon black (CB) as the reinforcing filler, with over 92% output intended to tire fabrication (Figure 1a,c).[2]

Tires are usually manufactured from a blend of rubbery polymers (e.g., polyisoprene, styrene−butadiene rubber, polybutadiene) mixed with additives, curing agents, and reinforcing fillers, all of which contribute to the unique mechanical and rheological properties.[3−5] Alongside silica ($SiO_2$), CB is the most performing filler for automotive applications.[6] However, its production is based on petroleum feedstock combustion such as hydrocarbons and aromatic

Received: June 4, 2025
Revised: August 26, 2025
Accepted: August 27, 2025
Published: September 5, 2025

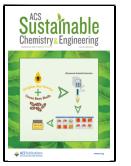

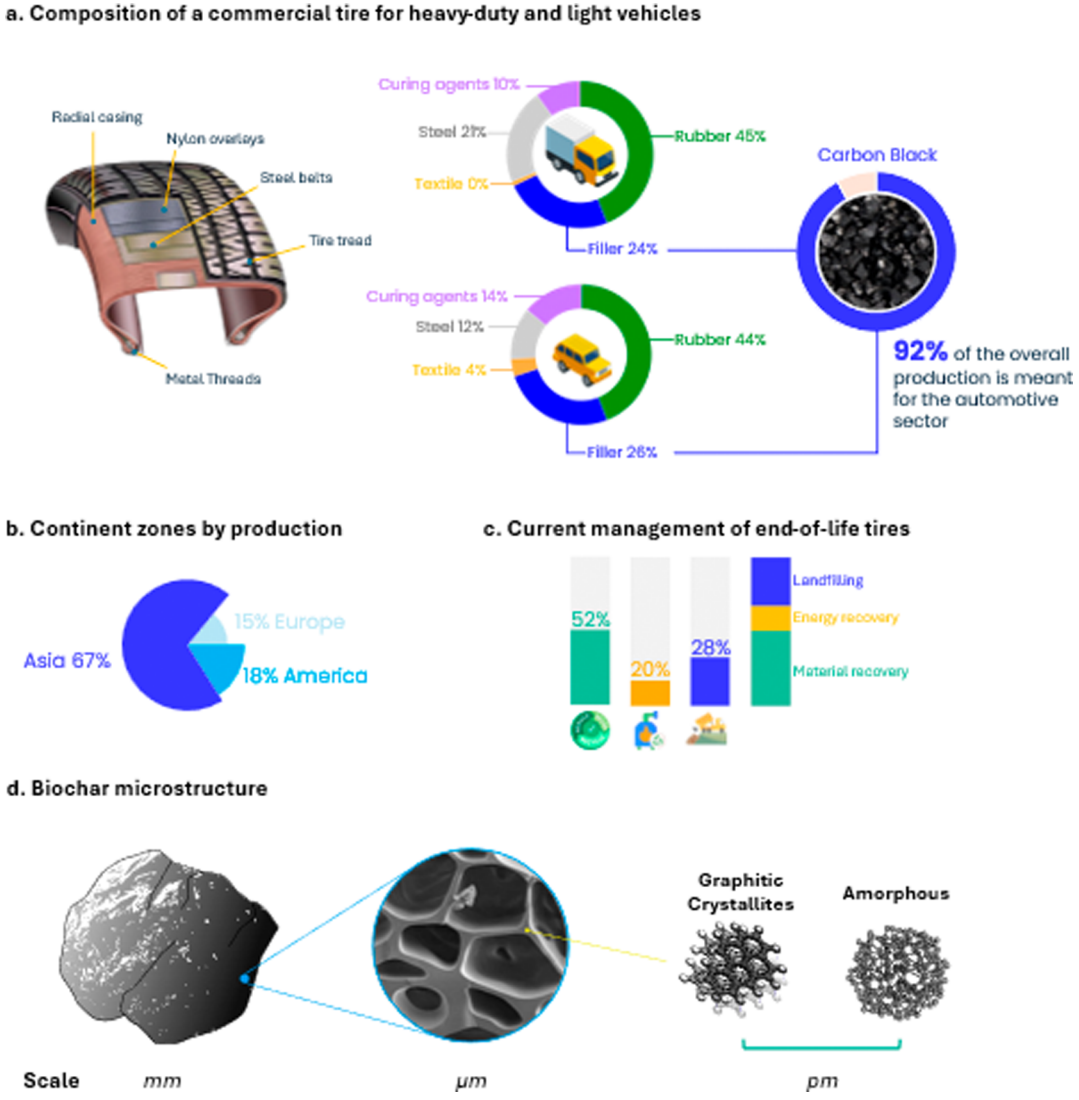


**Figure 1.** (a) Composition of commercial tires, (b) volume production of tires per continent zone, (c) current management strategies for dealing with end-of-life tires, and (d) schematic illustration of the biochar microstructure.

compounds, which poses significant environmental concern.[1,3,7,8] The intrinsic fossil nature of CB is responsible for 20% of greenhouse gas (GHG) emissions related to the transportation and automotive sectors, which are forcing companies to find alternative solutions in the contemporary decarbonization scenario.[2,9]

In response, efforts to mitigate the CB's environmental impact in the tire industry have led to alternative solutions. As per the current state-of-the-art in tire composite development, recycled char derived from discarded tire pyrolysis is gaining increasing attention and represents a fair alternative to end-of-life tire disposal problems. This approach allows us to obtain a char with high CB content with similar or even better reinforcing properties and reduced environmental footprint.[10−12] Recycled CB (rCB) is an example of waste upcycling, promoting tire recovery and decreasing virgin CB utilization. Despite these advantages, the rCB still relies on petroleum-derived materials and thus does not fully eliminate fossil fuel dependence.[10−13]

Other carbon-based materials, such as graphene,[14] graphite,[15] graphene oxide,[16] and carbon nanotubes,[17] have been explored as alternatives to CB in tire formulations due to their exceptional reinforcing capabilities. Nevertheless, challenges related to technology limits, high costs, and low production volumes hinder their applicability on an industrial scale.

In virtue of their abundance, low cost, and structural variety, biomass-derived fillers have emerged as attractive CB replacements in tire formulation.[5,18−20] In particular, various techniques have been developed to recover nanostructured cellulose in an appreciable yield. Mechanical shredding can reduce cellulose fibers from micro- to nanometric size through cleavage of microfibril arrangement found in natural cellulose sources.[21−23] Chemical hydrolysis, usually performed by acid or metal catalysis, allows extracting cellulose nanocrystal (CNC) by selectively decomposing the amorphous region of cellulose assembly.[23] Still, CNC implementation faces important challenges that limit its utilization in polymer materials. Despite their potential, CNCs face major challenges in polymer applications. Their low dispersibility in elastomer matrixes, above all, represents the principal hindering factor due to aggregation of primary particles mediated by intramolecular hydrogen bonding between cellulose glycosidic units.[24−26] Addressing this issue is complex as other factors come into play when evaluating the reinforcing properties.


https://doi.org/10.1021/acssuschemeng.5c05447
ACS Sustainable Chem. Eng. 2025, 13, 15421−15434

Primary, morphological parameters, such as particle dimension, surface area, and aggregate structure, and then chemical factors, like hydrophilicity, rule filler−matrix compatibility and consequently affect mechanical properties. Thus, plenty of structural and surface modifications (oxidation,[27] acylation,[28] esterification,[22] and silane coupling[19]) have been proposed to improve cellulose-based filler compatibility with convincing results.[24,25,29,30]

Similarly, agricultural residues are potentially suitable for tire manufacture due to their large-scale production and alignment with circular economy policies.[5,19,31,32] Unlike CNC, these biofillers represent a form of biomass readily available and desirable for their upcycling potential. Commonly referred to as biofillers, this class of fillers shares not only similar properties to nanocellulose but also different drawbacks caused by their uneven morphology and nonfixed composition.[18,33]

Pyrolyzed biomass, often referred to as biochar,[34] took this concept a step further, representing the link between carbonaceous and biomass-derived fillers. Indeed, biochar can be classified as a carbonaceous filler due to its structural similarities to CB.[35,36] Especially biochar derived from agricultural residues has been studied in tire formulations, demonstrating its potential as a filler.[20,37] Biochar is a paracrystalline material, rich in graphitic-like structures, incorporated into an amorphous phase capable of organizing into higher-order three-dimensional aggregates.[13] However, biochar's properties can vary significantly based on the feedstock and pyrolysis conditions used in its production. Lignocellulosic biomass is the primary source for biochar production, due to its widespread availability and low competing use in other sectors.[38]

Like other biofillers, biochar's composition can differ largely on the way it has been produced, resulting in a substantial difference in morphology from one biochar to another. Since the reinforcement of rubber composites considerably relies on filler morphological parameters, the mechanical enhancement relies mainly on surface area, particle size, aspect ratio, porosity, and surface chemical groups.[1,6] Still, the precise correlation between these parameters and mechanical properties remains unclear, limiting their application in the tire industry. Generally, an increase in filler surface area is associated with an enhanced reinforcement capability. This trend is especially true for commercial CB, where different grades are classified depending on average particle size and surface area.[1,39] However, in the biochar case, the relationship between morphology and mechanical properties is more complex.[5,38] The production process, raw material feedstock, and chemical surface chemistry all contribute to significant variability within the same biochar class.[11,35,36] In this case, however, the pyrolysis temperature is the key factor that influences the mechanical properties. Increasing the pyrolysis temperature enhances the growth of graphitic structures in the material, causing a shift in carbon content. Consequently, H/C and O/C ratios differ within the same biochar families, affecting particularly their morphology (Figure 1d).[36,40]

While prior studies, as per Dumont et al.,[37] have already explored the potentialities of biochar as replacement for CB in the elastomeric matrix, they usually focus on a limited biochar source selection, and they do not offer a comprehensive evaluation of the role of biochar structural parameters played in rubber reinforcement. Therefore, this study aims to comprehensively understand how different biochar microstructures affect mechanical and rheological properties, by offering a structure−property relationship linking biochar chemostructural parameters to the final mechanical performances of composites. In doing so, we selected biochar from different natural sources treated in identical pyrolysis conditions but characterized by diverse pore sizes, surface areas, particle dimensions, and surface chemistries. These biochars were incorporated in a commercial tire formulation by replacing CB in different ratios (30, 50, and 70 phr), the final composites were tested, and a model of their reinforcing mechanism was proposed based on the results obtained.

## EXPERIMENTAL SECTION

**Materials.** Natural rubber (NR, *Hevea brasiliensis*), styrene−butadiene rubber (SBR), sorbic acid (SA), ZnO, carbon black (CB, N326), oil, sulfur (S), and N-*tert*-butyl-2-benzothiazolesulfenamide (TBBS) were supplied by Michelin S.p.A (Cuneo, Italy) and used as received. Biochar derived from the pyrolysis of *Brassica napus* (oilseed rape straw, $OSR_{700}$ and $OSR_{550}$), *Miscanthus* (miscanthus straw, $MSP_{700}$), and *Gymnosperm* wood (softwood pellets, $SWP_{700}$) were supplied by the UK Biochar Research Center (Edinburgh, UK). Biochar was dried in an oven at 100 °C for 24 h, ground in a ball milling apparatus with iron steel balls over 24 h, and sieved at 150 $\mu$m prior to its use. Biochar properties such as surface area, H/C and O/C ratios, and biochar yield were derived from the technical datasheet provided by the research center and are available to the corresponding Web site.

**Composites Preparation.** Rubber composite formulations were prepared following a modified industrial recipe, which was used as a template. NR (11.2 g) and SBR (11.2 g) were added to an internal mixer (Brabender, Anton Paar GmbH, Graz, Austria) at a constant shear rate of 90 rpm and 120 °C. The rubber mixture was masticated from 5 to 10 min, until forming a homogeneous mass. After that, a ZnO (1.4 g) activator was added, followed by SA (0.56 g), working as a homogenizer, and mixed for an additional 5 min until it was well incorporated. Then, CB (11.2 g) was added in two rounds, followed by oil (4.48 g) to facilitate CB incorporation and dispersion. In the case of biochar-based formulations, part of the overall CB was replaced with biochar and added in this phase until it was well incorporated in the matrix. Once the second half of fillers and oil were added, the mixture was masticated for another 5 min, and eventually, S (0.448 g) and TBBS (0.672 g) accelerator were added and mixed until the mixture was dispersed uniformly. Eventually, the mass was extracted by the internal mixer and placed in a hot press (Laboratory Press-Drive, Gibitre Instruments S.r.l, Bergamo (BG), Italy) for 15 min at 100 bar and 140 °C to trigger the vulcanization. The resulting composites appeared as 3 mm thick discs. The mixing rate was never modified during the preparation. All the formulations included 100 phr of filler overall relative to the amount of rubber used; Table S4 (Supporting Information) summarizes all the formulations prepared in this study.

**Tensile Testing.** Dumbbell-shaped specimens of 30 × 4 × 2 mm ($l \times w \times t$) were obtained with a standardized punch cutter (AMSE S.r.l, Torino (TO), Italy) from the vulcanized composites. The specimens were then tested in tensile mode on an extensometer (Instron Universal testing Machine, Ulm, Germany) at a constant pace of 200 mm/min in triplicate (Table S5).

**Hardness.** Hardness (Shore A) was measured with a durometer (Shore A, S.A.M.A. Italia, Viareggio (LU), Italy) in quintuplicate.

**Payne Effect Measurements.** The Payne effect was measured with a modular compact rheometer (MCR 702e MultiDrive, Anton Paar, Ganz, Austria) in a parallel-plate configuration. Disks of unvulcanized rubber of 3 mm thickness were used as specimens and tested in amplitude sweep mode applying a normal force of 10 N and varying the shear strain $\gamma$ from 0.01% to 100% at a constant temperature of 100 °C and a frequency of 1 Hz.

**Dynamic Mechanical Analysis (DMA).** Glass transition temperature was determined by DMA on a modular compact rheometer (MCR 702e MultiDrive, Anton Paar, Ganz, Austria) in a tensile


https://doi.org/10.1021/acssuschemeng.5c05447
ACS Sustainable Chem. Eng. 2025, 13, 15421−15434

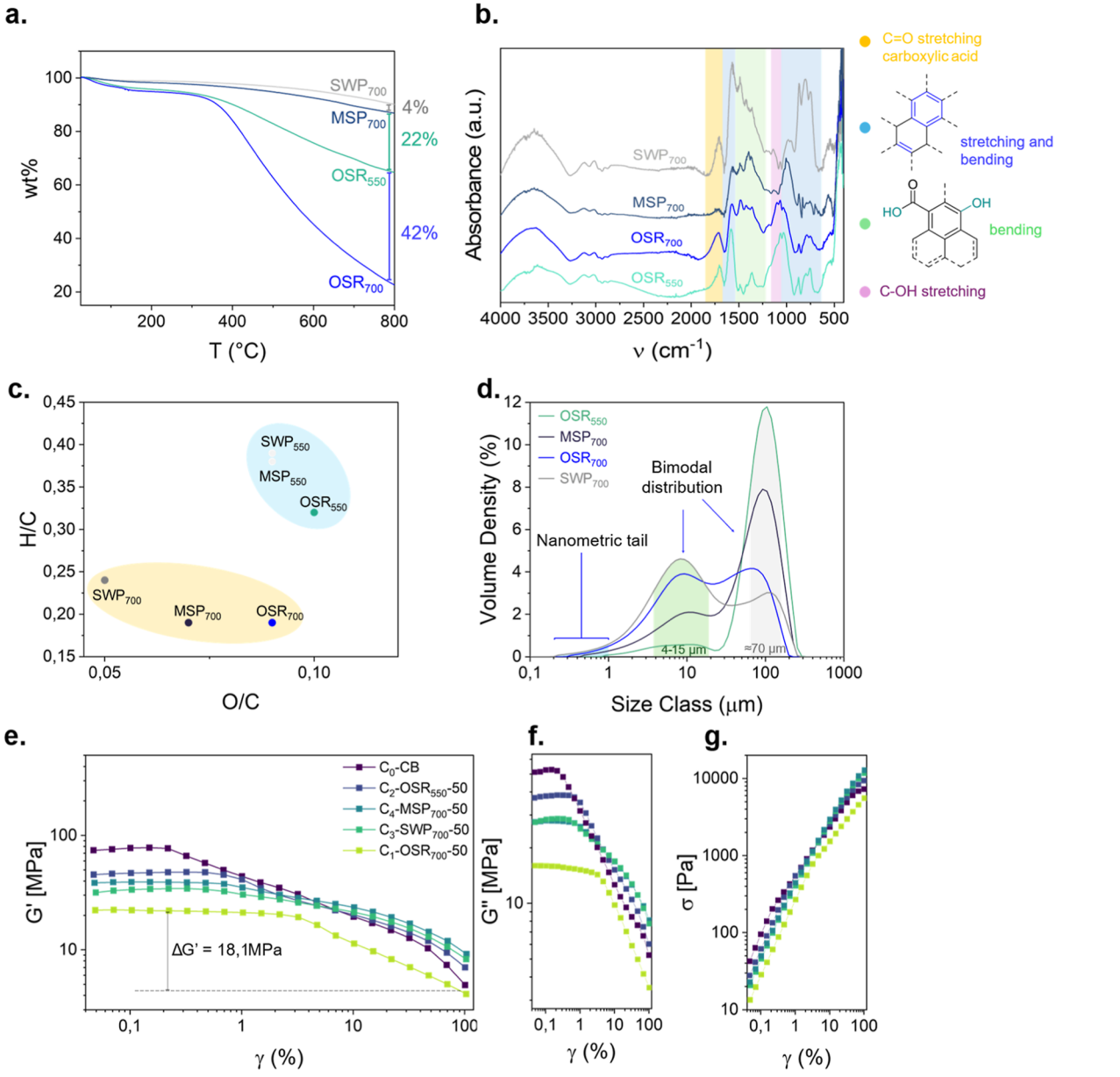


**Figure 2.** Characterization of the pristine biochar filler. (a) Thermogravimetric Analysis (TGA) of biochars recorded in an Ar atmosphere. (b) FTIR-ATR spectra recorded at 32 scans with a 4 $cm^{-1}$ resolution. The main superficial groups are shown on the side, with the relative frequency number intervals (1750−900 $cm^{-1}$). (c) van Krevelen diagram derived from biochar datasheet tables. Pyrolysis temperature marks two main clusters differentiated based on aromaticity; the 700 °C-treated biochars (yellow one) are characterized by a higher aromaticity degree. (d) Particle size distribution of biochar samples determined by Dynamic Light Scattering (DLS). Variation of (e) G′, (f) G″, and g) shear stress ($\delta$) at increasing shear strain ($\gamma$%) for NR/SBR composites at 50 phr. The curves present the so-called Payne effect, shown as a deviation from linear behavior in filled elastomers.

configuration. Samples of 20 × 5 × 2 mm ($l \times w \times t$) were cut from the vulcanized specimen at 50 phr and tested in a temperature sweep ranging from −75 to 65 °C. Loss (E″) and storage (E′) moduli were recorded in the linear viscoelastic region (0.1% extensional strain) at a frequency of 1 rad/s, from which tan $\delta$ values were derived and plotted versus temperature.

Cross-Linking Density Calculation: From the DMA test performed on composite samples at 50 phr, it was possible to calculate the cross-linking density from the storage modulus values (E′) at 25 °C by using eq 1:[41−43]

$$\eta = \frac{E'}{6RT} \quad (1)$$

where $\eta$ is the cross-link density (mol $cm^{-3}$), E′ is the elastic storage modulus (MPa), $R$ is the universal gas constant (J $mol^{-1}$ $K^{-1}$), and $T$ is the absolute temperature (K).

**Thermogravimetric Analysis.** Thermograms of the biochar rubber composite and pristine biochar were recorded on a thermal analysis system (TGA, Mettler Toledo, Columbus (OH), USA) with an alumina pan (150 $\mu$L) within a temperature range of 25−800 °C, at 10 °C/min in an Ar (50 mL/min) atmosphere to determine both the biochar and the resulting composite degradation pathways. Thermographs were normalized versus sample weight, and the first derivative graphs were calculated using Origin 2021 software using a Savitzky−Golay smoothing curve.

**Scanning Electron Microscope.** Biochar micrographs were collected on a scanning electron microscope (Phenom XL Scattering Electron Microscope, Thermo Fischer Scientific, Waltham (MA),



https://doi.org/10.1021/acssuschemeng.5c05447
ACS Sustainable Chem. Eng. 2025, 13, 15421−15434

USA) at different magnitude scales. Samples of pristine biochar were placed on stub and used without prior Pt sputtering.

Further information about biochar particle size distribution, Brunauer–Emmett–Teller, FTIR-ATR, and SEM micrographs is available in the Supporting Information.

## RESULTS AND DISCUSSION

A recent study on biochar replacement in rubber composite has already been reported by Dumont et al., in which they developed and characterized a series of corn-based biochars with the aim of replacing CB N772 in styrene–butadiene rubber (SBR) formulation.[37] Although reaching satisfactory reinforcing properties, they limited the study to a fixed 55 phr formulation without including CB as the cofiller or investigating other biochar sources. Having this base, this study explores not just the applicability of multiple biochar feedstocks in the NR/SBR matrix but also how the reinforcement level of such a filler varies by gradual CB replacement levels. The biochar selection relied on industrial-tailored ones in trying to establish a comprehensive relationship on the role of surface chemistry and morphology in polymer–filler interaction, aiming to formulate a realistic reinforcement model for biochar fillers.

The biochars used in the presented study were kindly supplied by the UK Biochar Research Center and were selected based on their total surface area and H/C and O/C ratios, which eventually led to an estimation of their aromatic degree[35,36] (Figure 2c). By the examination of the technical datasheet (Table S1, Supporting Information), biochars derived from *B. napus* (oilseed rape straw, OSR), *Miscanthus* (miscanthus straw, MSP), and *Gymnosperm* wood (softwood pellets, SWP) families, all produced by pyrolysis at 700 °C, were selected. These samples were in the lower portion of the van Krevelen diagram in Figure 2c. The lower H/C ratio compared to the wide O/C ratio range of these biochars was thought to behave differently based on their characteristic aromaticity and surface chemistry. Additionally, an OSR sample pyrolyzed at 550 °C was included in the selection to evaluate the effect of pyrolysis temperature, as it exhibited a lower H/C/O/C ratio compared to MSP and SWP analogues. Each biochar sample was finely ground through ball milling and sieved prior to its utilization to remove bigger chunks or agglomerates. The processed biochars were then incorporated as a filler in a standardized formulation of natural rubber (NR, *H. brasiliensis*) mixed to SBR, replacing CB at loadings of 30, 50, and 70 phr (Table 1). Finally, a comprehensive characterization of the aforementioned biochar was carried out alongside mechanical and rheological analyses on the resulting rubber composites.

**Biochar Superficial Characterization.** FTIR spectroscopy was used to investigate the biochar surface chemical groups. The vibrational bands of each sample were assigned according to the IR table in the literature, and the spectra are plotted in Figure 2b for comparison. Peak assignment was crucial to reconstructing the superficial functional groups involved in the interaction with the rubber matrix. The broad band at 3640 $cm^{-1}$ was related to the stretching vibrational mode of hydroxy (−OH) groups, while lower-intensity peaks at 3120−3025 $cm^{-1}$ belong to the C=C−H stretching of alkene moieties, and the small band at 2912 $cm^{-1}$ highlights the presence of alkane C−H stretching modes. The identification of such vibrational bands can be attributed to the para-crystalline C structure of biochar, with saturated and unsaturated groups

**Table 1. Chemical Composition of NR/SBR Composites Used in This Study**

| materials | $C_0$-reference | | $C_n$–biochar | | |
|---|---|---|---|---|---|
| | | | phr | | |
| NR | | | 100 | | |
| SBR | | | 100 | | |
| ZnO | | | 5 | | |
| SA | | | 2 | | |
| oil | | | 40 | | |
| S | | | 4 | | |
| activator | | | 6 | | |
| CB | 50 | 100 | 70 | 50 | 30 |
| biochar | | | 30 | 50 | 70 |

equipped by hydroxy R−OH groups giving rise to an intramolecular interplay. The presence of a carbonyl C=O peak was indicated by the band at 1705−1730 $cm^{-1}$, likely related to carboxylic groups (acids and ethers) formed during the pyrolysis. The presence of both bands at 1470 $cm^{-1}$ (carboxylic acid and alcohols O−H bending) and 1362 $cm^{-1}$ (phenol O−H bending) confirmed the presence of oxygenated functionalities (phenols, carboxylic acids, alcohols) as the main surface groups. Significant were the bands at around 1575 $cm^{-1}$, typical of C=C stretching modes of aromatic groups and cyclic alkenes.[35] Finally, bands at 1070−1030 $cm^{-1}$ were assigned to C−O bending modes of primary alcohol, while bands at 1010−960 $cm^{-1}$ and 850−730 $cm^{-1}$ were related to the C=C−H bending of tri/disubstituted alkenes, respectively, in trans and cis configurations.[44] Overall, even though each biochar shows similar vibrational bands, peak intensities vary from one another by virtue of the lignocellulosic feedstock content and the pyrolysis temperature. Particularly, it could be deduced that for $SWP_{700}$ and $MSP_{700}$, alcoholic groups formed in a lower amount compared to the OSR class by the lower peak intensity of the C−OH band, pointing to the first main difference in filler surface functionalities. $OSR_{550}$, instead, presents a lower inclusion of phenolic and carboxylic acid groups due to the absence of bands in the 1300−1400 $cm^{-1}$ window. Additionally, it must be noted that within the 1400−1000 $cm^{-1}$ range lie also low-intensity bands of aromatic/aliphatic esters and ethers' C−O stretching that overlap with O−H bending bands.[45,46] Ether and esters are most likely present in all biochar structures but not in the presence of $OSR_{550}$, which indicates that carboxylic acid derivatives form at higher pyrolysis temperatures. Similarly, the bands related to unsaturated (alkene and aromatic) structures have higher intensity for $SWP_{700}$, which is possibly characterized by higher-order graphitic structures. An explanation for this difference can be attributed to the higher lignin content in softwood feedstock compared to oilseed and miscanthus.[45] Ultimately, the FTIR assignment helped us to outline the superficial chemistry of biochar fillers along with their structural features. Overall, similarly to CB, biochar para-crystalline structures present a $\pi$-system with some degree of aromaticity, including oxygen-containing groups along graphitic layers. The surface groups not only have a coparticipation in aggregate organization in virtue of the inter-/intralayer bonding interaction (i.e., van der Waals, London, Hydrogen bonding) but also play a pivotal role in filler–matrix interaction when used as a filler in rubber formulations.[47,48] Considering the varying percentages of alcohol, esters, ethers, and phenolic groups in these four classes, the reinforcement effect will be



https://doi.org/10.1021/acssuschemeng.5c05447
ACS Sustainable Chem. Eng. 2025, 13, 15421−15434

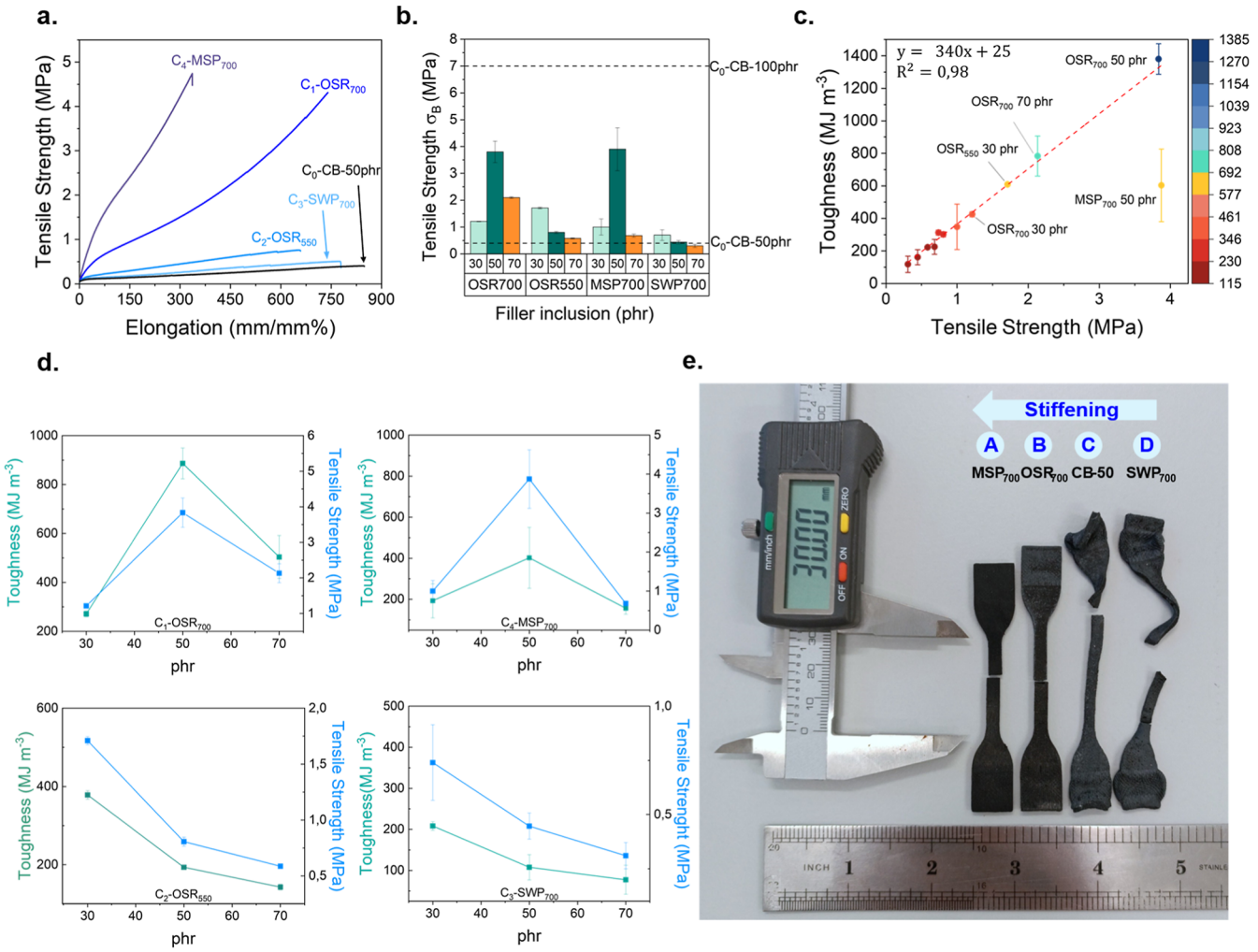


**Figure 3.** (a) Stress−strain curves recorded for biochar composites at 50 phr. (b) Bar plot diagram summarizing tensile strength recorded from stress−strain curves for every composite. Data were collected in triplicate to have a statistical evaluation of composite strength. (c) Toughness vs strength plot with the corresponding linear fitting equation. Toughness data showed a linear correlation to strength in all cases except for MSP700 at 50 phr, which resulted in an outlier. (d) Toughness/Strength trends vs filler inclusion (phr). (e) Picture of composite samples at 50 phr postbreaking, showing a permanent deformation (C,D) and a stiffer rubber behavior (A,B).

affected by the interaction between surface groups and the rubber matrix, in addition to particle size and surface area.

Particle size distribution of biochars is reported in Figure 2d. Notably, for OSR biochars, a higher pyrolysis temperature led to a finer particle size distribution, indicating that increasing the treatment temperature of biomass can reduce particle size. This trend is clearly observed when comparing $OSR_{550}$ and $OSR_{700}$. $OSR_{550}$, produced at a lower pyrolysis temperature, exhibited the largest median particle size ($d_{50}$ = 92.0 $\mu$m) among the analyzed samples, whereas $OSR_{700}$ had a significantly reduced median size ($d_{50}$ = 19.2 $\mu$m). A similar effect of pyrolysis temperature on particle size reduction has been reported in the literature, where higher thermal decomposition enhances particle fragmentation due to the breakdown of biomass structural components. Additionally, biomass types have a distinct influence on particle size distributions (Table S2). The particle size variations among biochars have been attributed to differences in the biomass composition and structural integrity.

Microstructural analysis of biochar was completed by the average pore size and surface area evaluation by isothermal absorption−desorption studies, and the results can be found in Table S3 of the Supporting Information. Instead, thermogravimetric analysis (TGA, Figure 2a) was carried out in an Ar atmosphere to derive degradation curves at high-temperature regimes. The presence of a drop at around 100 °C is a symptom of the hygroscopic nature of the OSR biochar, which loses up to 5% of its initial weight in adsorbed water. Seemingly, $SWP_{700}$ and $MSP_{700}$ did not present any consistent thermal degradation in contrast to the OSR biochar, for which the residual weight was assessed on 50% of the initial sample. This behavior has been attributed to oxygenated group leaching at 400 °C, where mostly phenolic, carboxylic, ester, and ether groups degrade, leading to weight loss. This result is in good agreement with the van Krevelen diagram, where the biochar of the OSR presents the highest O/C ratio.

**Microstructural Interpretation of Polymer−Filler Interaction.** Filled elastomers have a strong dependence of storage modulus (G′) on dynamic deformations, decreasing with an increasing shear strain amplitude. This nonlinear phenomenon in elastomer composites (Figure 2g), known as the Payne effect, is attributed to the disruption and reformation of the filler network above the percolation threshold.[49−51] The magnitude of the Payne effect serves as a crucial indicator of



https://doi.org/10.1021/acssuschemeng.5c05447
ACS Sustainable Chem. Eng. 2025, 13, 15421−15434

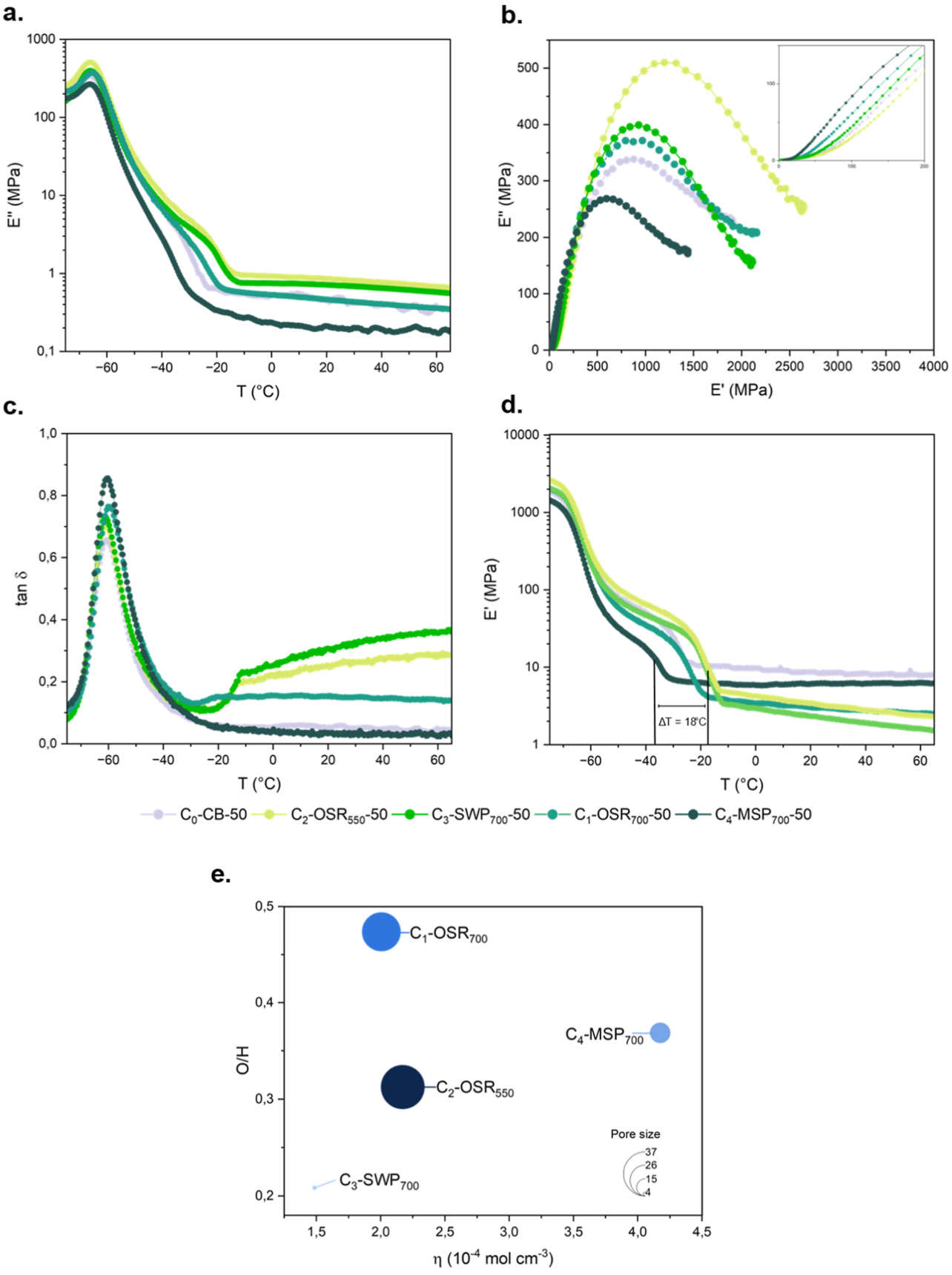


**Figure 4.** DMTA curves measured for NR/SBR biochar composites at 50 phr (named $C_x$-Biochar-50) inclusion: (a) E″, (b) Cole−Cole diagram expressed as E″ vs E′, (c) tan $\delta$ and (d) E′ as a function of temperature, and (e) bubble plot presenting the cross-linking density of 50 phr composites correlated to biochar pore size and O/H ratio.



https://doi.org/10.1021/acssuschemeng.5c05447
ACS Sustainable Chem. Eng. 2025, 13, 15421−15434

Table 2. Summary of Mechanical Data Recorded from Tensile Machine for NR/SBR Composites and of Crosslinking Density Calculated from DMA Curves

| composite | biochar (phr) | Young's modulus (MPa) | $\varepsilon_B$ (%) | $\sigma_B$ (MPa) | $\eta$ ($10^{-4}$ mol cm$^{-3}$) |
|---|---|---|---|---|---|
| $C_1$−$OSR_{700}$ | 30 | 23 | 655 | 1.21 | |
| | 50 | 23.2 | 789 | 3.8 | 2,0 |
| | 70 | 23 | 736 | 2.1 | |
| $C_2$−$OSR_{550}$ | 30 | 24 | 717 | 1.71 | |
| | 50 | 24.3 | 663 | 0.80 | 2,2 |
| | 70 | 24 | 629 | 0.58 | |
| $C_3$−$SWP_{700}$ | 30 | 20 | 694 | 0.7 | |
| | 50 | 21.9 | 677 | 0.44 | 1,5 |
| | 70 | 21.7 | 667 | 0.30 | |
| $C_4$−$MSP_{700}$ | 30 | 23.0 | 518 | 1.0 | |
| | 50 | 23.7 | 271.3 | 3.9 | 4,2 |
| | 70 | 23.9 | 653 | 0.68 | |

polymer−filler interaction and can help elaborate a microstructural interpretation of biochar reinforcement.[52] In Figure S2, the G′ vs strain ($\gamma$%) graph presents the Payne effect recorded for biochar composites in their unvulcanized state at increasing filler inclusion with respect to reference $C_0$-CB (Table S4). Composites with higher initial G′ values suggest a more rigid filler network, associated with stronger filler−filler interactions and reduced polymer mobility. Generally, the initial G′ decreases at higher CB replacement for all samples. However, $C_3$−$OSR_{550}$ did not present the same trend, for which initial G′ increases at 50 phr but eventually decreases at a high biochar replacement of 70 phr. It must be noted that the initial G′ recorded for biochar composites was lower compared to the $C_0$-CB reference in all cases. The effect highlighted on the biochar replacement percentage can be easily ascribed to the weakening of the filler network due to the decrease in CB content (Figure 2e,f). The modulus drop observed at strain levels between 1% and 10% is typical of a composite with a higher filler−filler interaction degree in the initial state, undergoing a subsequent decline under increasing strain. At higher strain regimes ($\gamma$ > 10%), the residual G′ reflects polymer−filler interactions existing within the matrix.[52−55] According to Figure 2e and Figure S2, $C_1$−$OSR_{700}$-50 modulus drop ($\Delta G' = G_0' - G_\infty'$) happens at higher $\gamma$%, suggesting a retarded filler network collapse compared to other samples. The lowest $\Delta G'$ recorded in the $C_1$−$OSR_{700}$ case is a consequence of a filler−polymer network with increased mobility for the reduced CB loading. The conflicting results stem from the apparent different reinforcing mechanisms of biochar, where morphology influences filler−rubber entanglement, in contrast to the nanometric CB, which forms filler architectures that hold tightly entangled chains.[1,6,49,52] Similar considerations can be applied to other samples. Overall, biochar composites exhibit a filler−polymer microstructure distinguished by increased polymer mobility with a weaker filler network. Reasonably, composites with a pronounced Payne effect are associated with the worst filler dispersion as the increased filler−filler interaction may be detrimental for the overall reinforcement.[55] Consequently, $C_1$−$OSR_{700}$ is expected to have optimal dispersion and a balanced percolated network, as discussed. The decrease in $\Delta G'$ at 70 phr replacement, instead, develops an unstructured CB network that further weakens the filler network; therefore, the resulting composites were expected to provide a limited or poor reinforcement.

**Composite Reinforcement Behavior.** Mechanical properties were our primary focus for composite reinforcement evaluation and filler activity estimation. To optimize biochar inclusion, we tested composite resistance on a dynamometer in tensile mode. Figure 3b presents the bar plot where the stress recorded at breaking ($\sigma_B$) of the specimen was plotted versus filler content. The formulation $C_0$-CB (Table S4) was considered as the standard reference to evaluate the effect of gradual filler replacement on NR/SBR composites. Tensile strength trends led us to observe that reinforcement did not occur in the same way for every biochar class. Indeed, two different behaviors could be highlighted. $C_2$−$OSR_{700}$ and $C_3$−$MSP_{700}$ composites displayed a strengthening effect in moving from 30 to 50 phr of filler inclusion, with the maximal tensile strength of 3.9 MPa recorded at 50 phr of $C_4$−$MSP_{700}$ (Table S5). Further inclusion of biochar at 70 phr affects the mechanical properties, lowering the tensile strength to 0.68 MPa. Weakening of the rubber composite at higher filler inclusion can be attributed to the lack of CB, which decreases from 70 to 30 phr. Ground $OSR_{700}$ and $MSP_{700}$ biochars are characterized by granules of 3 orders of magnitude bigger than CB, staying in the range of 15−50 $\mu$m (Figure S5). As the inclusion of micrometric particles results in a higher percentage of agglomerates in the composite network, it reduces dispersion and filler−matrix interaction. $C_1$−$OSR_{700}$, however, recorded a tensile strength of 2.1 MPa, comparably higher than those of the other biochar families. On the contrary, $C_2$−$OSR_{550}$ and $C_3$−$SWP_{700}$ composites weakened greatly at 50 and 70 phr (Figure 3d), revealing an overall detrimental effect on the NR/SBR network (Table S5). $SWP_{700}$ composites were expected to have the best performance due to the extremely high surface area (Table S3) in the first place. However, tensile strength decreases from the initial 0.7 MPa (30 phr) to 0.3 MPa (70 phr), indicating no reinforcement was provided by biochar in this case. We observed that $SWP_{700}$ composites exhibited viscous sliding during elongation with barely any elastic return after breaking. Similar arguments apply for the $OSR_{550}$ composites, which eventually did not show the typical rubbery behavior. This behavior can be better explained looking at Figure 4e, where the relationship between composites cross-linking density and biochar parameters has been highlighted. The $SWP_{700}$ filler addition negatively influences the cross-linking density ($1.4 \cdot 10^{-4}$ mol cm$^{-3}$), which is probably ascribed to the reduced pore size and worse interaction with the matrix, while the addition of the $OSR_{550}$ led to a composite's cross-link density comparable with the one achieved by the $OSR_{700}$ ($2 \cdot 10^{-4}$ mol cm$^{-3}$), consistent with its higher average pore size. However, $OSR_{550}$ lower superficial


https://doi.org/10.1021/acssuschemeng.5c05447
ACS Sustainable Chem. Eng. 2025, 13, 15421−15434

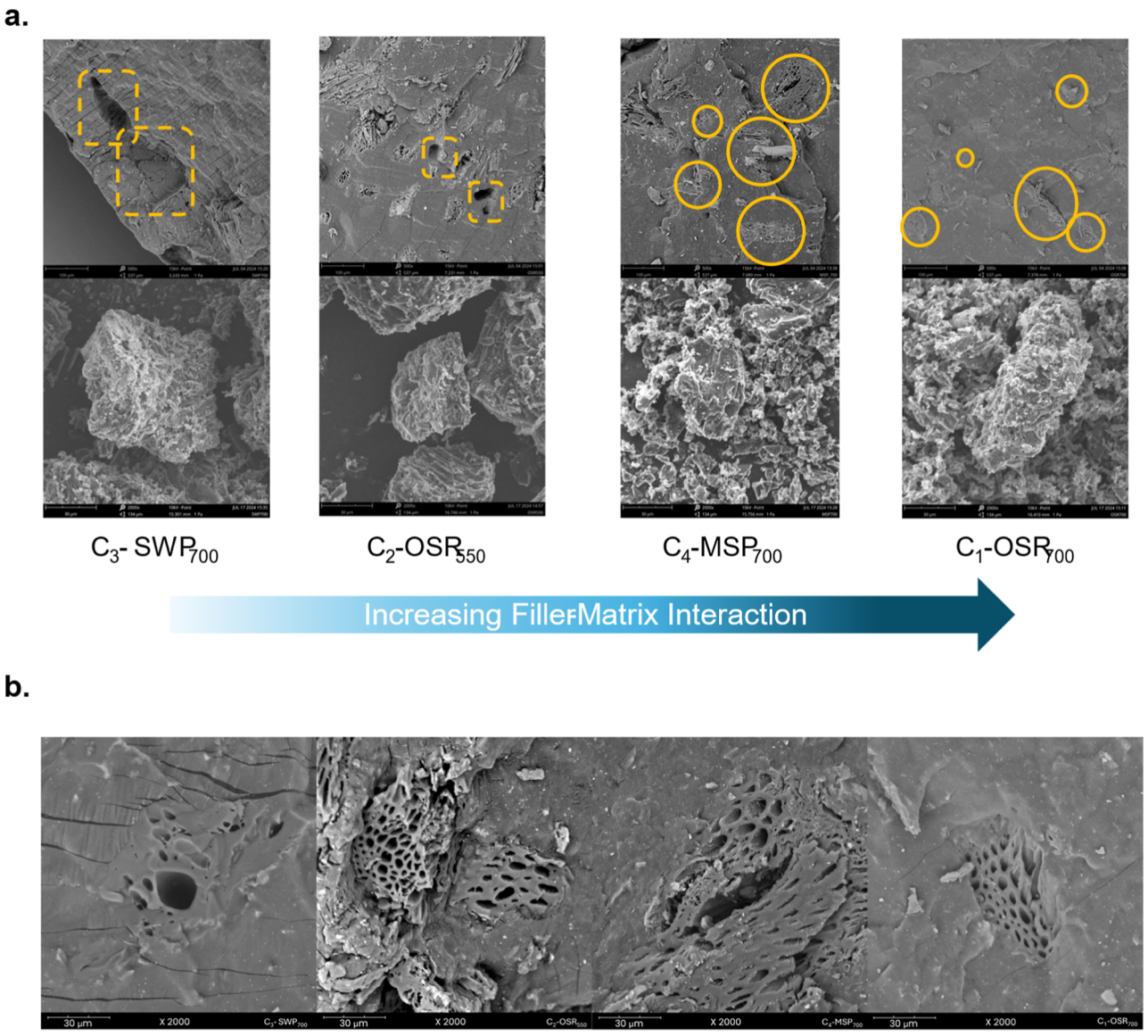


**Figure 5.** SEM micrograph of biochar composites. (a) Fracture surface at ×500 (top) compared to pristine biochar powder (bottom) to have an insight into a pull-out phenomenon. (b) Fracture surface at ×2000 magnification showing how biochar granules disperse and interact with the matrix. The presence of cracks and splits around filler particles (Figure 5b) was another counterproof of the poor filler−matrix interaction in $OSR_{500}$ and $SWP_{700}$ composites. These microruptures are a consequence of the fracturing event, and the occurrence of it is not casual. Indeed, they are an index of energy absorption capabilities. As per $SWP_{700}$ (Figure 5b), microruptures develop around the filler grain, causing structural collapses, in virtue of the weak interaction. $OSR_{550}$, instead, tends to agglomerate into larger structures, which are visible also at lower magnification (Figure 5a), pointing to a low dispersion tendency. However, the presence of large agglomerate chunks hinders matrix reinforcement by forwarding uneven stress distribution. These conclusions confirm what already emerged from tensile tests that showed a decreasing trend for $OSR_{550}$ and $SWP_{700}$, moving from 30 to 70 phr formulations. On the other hand, $OSR_{700}$ and $MSP_{700}$ composites did not present the same phenomena with fillers included effectively in the rubber, as shown by the better dispersion and the characteristic sharp filler−matrix interface.

group affinity (expressed as the $\frac{O}{H} = \frac{\frac{O}{C}}{\frac{H}{C}}$ ratio herein) can lead to overstrain of the polymer's chains during the tensile test, and due to local strain amplification, the polymer matrix can reach locally its limit of extensibility. Consequently, chain breakage, chain detachment, or slippage at the polymer/filler interface occurs, thus leading to a loss of rubbery behavior.[56−58] Similarly, the overstiffening recorded in $C_4$−$MSP_{700}$ (Table 2) is a consequence of the greater cross-link density, which results from the higher O/H ratio in connection to a lower pore size compared to the OSR family. To further investigate this behavior, we prepared an additional tire mixture with only 50 phr of CB to assess whether even a minimal filler content would affect the rubber matrix (Figure 3a). The mechanical properties of these two composites were comparable to those of the unfilled rubber matrix (Table S5, $C_0$-CB-50), proving that the $OSR_{550}$ and $SWP_{700}$ composites made almost no contribution to the overall reinforcement. For these two cases, the decrease of mechanical performances is due solely to the decrease of CB content, leading us to conclude that the corresponding composites are not suitable for tire applications. This result was ascribed to a poorer and almost nonexistent reinforcing activity of $SWP_{700}$ and $OSR_{550}$, due to the lack of sufficient filler−matrix interaction.[56−58]


https://doi.org/10.1021/acssuschemeng.5c05447
ACS Sustainable Chem. Eng. 2025, 13, 15421−15434

Generally, biochar composites could not outperform $C_0$-CB-100 phr performances although they contributed to the overall reinforcement, working better than $C_0$-CB-50 phr (Figure 3b) in every case. From stress−strain curves (Figure 3a), the Young modulus was evaluated in the linear viscoelasticity range and is reported in Table 2, alongside with elongation at break ($\varepsilon_B$) and hardness (Shore A) values. Young's modulus ranged within 21−24 MPa, marginally lower compared to $C_0$-CB composites (Table S5), which reached 24.9 MPa, but largely comparable regardless of biochar content. This indication is corroborated by $\varepsilon_B$ and the hardness values. Elongation, especially, increases in all cases except for the $MSP_{700}$ composite at 50 phr, for which $\varepsilon_B$ was limited to 271%, while hardness reached 84 Shore A. Generally, hardness correlates with tensile strength values and reflects the reinforcing behavior of biochar; the sole exceptions are 50 phr composites of $MSP_{700}$ and $SWP_{700}$. The anticorrelation behavior of $MSP_{700}$ can be better visualized in Figure 3c, where toughness values were plotted against tensile strength. The toughness parameter is related to the ability of a material to absorb energy during loading and plastically deform before breaking, assuming the physical meaning of energy density stored in the material. Higher toughness is desirable in practical applications where stress propagation leads to critical failures and damage to the material structure. However, a balanced compromise between strength and ductility is not always straightforward to accomplish in polymer composites.[59] Tensile strength is inherently correlated with material toughness. Still, the two parameters are often mutually exclusive.[60,61] To our aim, therefore, we considered composite toughness as the watershed parameter for truly representing composite reinforcement by the biochar. The filler−matrix interfacial structure regulates the network resilience and serves as an additional point of entanglement for polymer molecules to withstand mechanical stimulation. Zeng et al. elucidated the role of the filler−matrix surface structure in polydimethylsiloxane (PDMS) Al-filled elastomer composites, ascribing high toughness and resilience to the entanglement phenomenon arising between polymer chain and dangling chain connected with the filler.[62] Similarly, the correlation between toughness and tensile strength, linked to filler morphological characteristics, provided us with crucial information on the biochar reinforcing mechanism. In Figure 3c, toughness vs tensile strength values shows a linear correlation with a high determining factor ($R^2$ = 0.98). Experimentally, the data are in good agreement with the linear regression fitting, except for the composite of $MSP_{700}$ (50 phr), for which the toughness of 603 MJ $m^{-3}$ turns it into an outlier. Reasonably, this behavior is typical of a stiffer rubber composite with limited extensibility and applicability in the tire industry. The highest toughness value was achieved for the $OSR_{700}$ at 50 phr (1380 MJ $m^{-3}$), which reconfirms superior mechanical properties. While the $OSR_{700}$ composite at 70 phr inclusion keeps a reasonable toughness of 783 MJ $m^{-3}$, $MSP_{700}$ remaining composites (30 and 70 phr) stay in the low toughness value range (>450 MJ $m^{-3}$, Figure 3c). Reasoning on filler morphological parameters, we postulated that the explanation behind this variability is 2-fold. First, the biochar mesoporous structure (2−50 nm) rules the interfacial interaction with the elastomer matrix, serving as a template for rubber chains to grasp filler particles/aggregates by entering the pores when in the unvulcanized state (>100 °C). However, rubber macromolecules are limited to enter pores of certain dimensions that stay within the mesopore range, meaning that biochar with a smaller pore size would likely forward poor reinforcement. In the second place, the nature of biochar superficial groups is known to regulate filler−matrix interaction by noncovalent bonding, mostly complex to rationalize for biochar but estimable by looking at the van Krevelen diagram (Figure 2c). Biochars pyrolyzed at 700 °C have a lower H/C ratio consisting of higher aromaticity compared to the ones pyrolyzed at 550 °C, which instead have a similar composition to the initial feedstock.[36] The lower aromaticity also returns a higher percentage of oxygenated groups, responsible for hydrophilic interactions and thus higher tendency to form agglomerates in the hydrophobic elastomer matrix. It follows that in the biochar present on the top-right part of the graph, the lack of aromaticity and the prominent hydrophilic character hinder filler dispersion and its interaction with the matrix. In contrast, the biochar present on the bottom-right part of the graph possesses the proper balance between oxygen-containing groups and degree of aromaticity as per the case of $OSR_{700}$ and $MSP_{700}$ that, coherently to SEM micrographs (Figure 5a,b), appear well dispersed within the rubber matrix. Mostly, these two are differentiated by the average pore size, according to the scale $SWP_{700}$ < $MSP_{700}$ < $OSR_{700}$ < $OSR_{550}$ (Table S3). $OSR_{700}$ and $MSP_{700}$ fall within the mesoporous range; however, $OSR_{700}$'s higher average pore size (32.8 nm) linked to the higher O/C ratio yielded greater reinforcement properties. This also justifies the loss of strength and ductility recorded for the $OSR_{550}$ (low aromaticity degree) and $SWP_{700}$ (small average pore size, 3.8 nm) (Figure 3d). Eventually, the deductive process based on such considerations led us to conclude that porosity is the primary factor ratio for biochar reinforcement at a similar O/C ratio, while particle size and surface area assume just a secondary role in filler−matrix interaction.

**Dynamic Thermal Analysis of Biochar Composites.** The viscoelastic behavior of composites was instead investigated by Dynamic Mechanical Thermal Analysis (DMTA). Particularly, Figure 4 presents dumping factor (tan $\delta$), tensile storage (E′), and loss modulus (E″) variation within the −70−0 °C temperature range for biochar composites at 50 phr, compared with the reference ($C_0$, Table S4). Below glass transition temperature ($T_g$), where the rubber network is completely frozen, there are no substantial influences on E′ and E″, eventually presenting similar trends at higher temperature regimes. Coherently, biochar did not have any consistent effect on $T_g$ which was recorded at −60 °C in all cases (Figure 4c); however, above the $T_g$ storage modulus, biochar composites reached the rubbery plateau at lower values compared to CB in all cases. The presence of a second drop in Figure 4a and d suggests a second glass transition attributed to the SBR phase in the composite. Usually, the SBR $T_g$ peak is found around −38 °C on the tan $\delta$-T plot;[37] however, the presence of a sole tan $\delta$ peak means that there was no thermodynamical NR/SBR phase separation,[39] but still a small transition relative to SBR could be highlighted on E′-T plots. This leads to the identification of two rubbery plateaus corresponding to NR/SBR (phase mixed) and SBR (separated). Interestingly, according to Figure 4d, there is an influence on SBR $T_g$ instead, with a substantial shift in the relaxation temperatures (−35 to −20 °C).

The E′ in the rubbery plateau region corresponds to the relative cross-linking density according to the classical theory of rubber elasticity.[63] In Figure 4d, biochar composites at 50 phr have slightly lower E′ compared to the CB reference, but


https://doi.org/10.1021/acssuschemeng.5c05447
ACS Sustainable Chem. Eng. 2025, 13, 15421−15434

still E′ was higher for $C_4$−$MSP_{700}$ above −20 °C, associated with a higher cross-linking density relative to the other samples. These considerations additionally suggest that replacement of CB with the biochar originates softer composites. On the other hand, loss modulus increased slightly except for $C_4$−$MSP_{700}$ for which E″ values decreased significantly already at $T_g$. The E″ assumes the physical meaning of mechanical energy dissipated to heat by internal friction during deformation. The increase in loss modulus in $C_2$−$OSR_{550}$ and $C_3$−$SWP_{700}$ has been attributed to energy dissipated by the breakdown of filler aggregates formed in the matrix, pointing to a major agglomeration tendency compared to $MSP_{700}$ and $OSR_{700}$ (Figure 4d). However, considering that E″ at 0 °C has been recognized as an indicator of tire wet grip,[3,39,64,65] the lower E″ for $C_4$−$MSP_{700}$, therefore, points out a smaller agglomerate formation as well as a reduced wet grip of the final composite.[65]

The dumping factor (tan $\delta$) was reported as a function of temperature in Figure 4c. Biochar inclusion in the formulation has a strong influence on the tan $\delta$ peak height; more precisely, the height increase is correlated to a decrease in CB and to the characteristic filler−filler network strength. The peak height is directly linked to filler dispersion for which a higher dispersion weakens the filler−filler network and decreases the amount of rubber entanglement with it. In a low CB composite, the biochar network is responsible for the macromolecules restriction in chain segment relaxation.[3,39] Consequently, $C_1$−$OSR_{700}$ and $C_4$−$MSP_{700}$ forward the highest peaks as a result of improved dispersion compared to $C_3$−$SWP_{700}$ and $C_2$−$OSR_{550}$. Additionally, rolling resistance and wet skid resistance can be interpreted from the tan $\delta$-T plot. The rolling resistance refers to the tire's opposition to motion and is caused by nonelastic effects such as hysteresis losses and permanent plastic deformations in the material. Usually, tan $\delta$ values at 60 °C give an estimation of rolling resistance for tire composites,[3] while wet skid resistance consists of another important safety parameter related to the wet friction acting during braking on wet surfaces. Since it is assumed that wet skidding happens at temperatures equal to or lower than room temperature, tan $\delta$ at 0 °C is taken as an indicator for wet skid resistance.[3] Figure 4c indicates that both rolling and wet skid resistances are higher in all cases compared to $C_0$-CB, except for $C_4$−$MSP_{700}$, where tan $\delta$ does not shift from the reference sample. This effect was expected in the case of $C_3$−$SWP_{700}$ and $C_2$−$OSR_{550}$ for which filler−filler networks exhibit higher adhesion consequently to aggregation. This behavior is actually undesired for energy consumption purposes as higher rolling resistance causes an increase in the power required by mechanical engines and therefore confirms that $SWP_{700}$ and $OSR_{550}$ are unsuitable fillers for tire manufacture as they cause loss in the usual rubbery behavior in replacing CB. However, $C_1$−$OSR_{700}$ gives a balanced compromise between the higher wet skid resistance and contained rolling resistance. Moreover, the higher tan $\delta$ in relation to the superior mechanical properties makes this material suitable for dumping applications.

By plotting loss modulus data (E″) as a function of storage modulus (E′), the Cole−Cole plot was obtained and is reported in Figure 4b. All composites are characterized by semicircular profiles, typical of a Maxwellian behavior.[66] Most importantly, the arc slope at low E′ has been reported as an indicative parameter for describing the polymer−filler interaction.[65] Lower slopes are diagnostic of an improved interfacial interaction. The Cole−Cole plot was considered as a final evaluation of the polymer−filler interaction in vulcanized samples. The inset in Figure 4b presents a slightly lower slope just for $C_2$−$OSR_{550}$ and tends to increase in all the other biochar composites. This result is a further indication that reinforcement for biochar cases is not just a matter of polymer−filler superficial adhesion but is determined by a different interaction model.

**SEM Micrographs Analysis.** Fracture-surface analysis of composites was performed by cracking vulcanized samples in liquid $N_2$ and by examining the fractured surface on SEM micrographs to evaluate the biochar dispersion. Composites at 50 phr of $OSR_{700}$, $MSP_{700}$, $SWP_{700}$, and $OSR_{550}$ were selected for optimal filler inclusion based on tensile properties, as determined by mechanical testing (see the next paragraph). Micrographs were taken at different magnifications in a backscattered mode to differentiate between included fillers and superficial residues or impurities. Images in Figure 5a give a clear indication of the filler affinity toward the matrix and were arranged from the least to the most akin. A stronger filler−matrix interaction was noticed for the $OSR_{700}$ and $MSP_{700}$, where tight filler−rubber blending was present around the interface (Figure 5b). $SWP_{700}$ and $OSR_{550}$ showed the worst inclusion in the matrix, which was also evident by the pull-out of large filler chucks on the fracture. The pull-out phenomenon was manifested especially for $SWP_{700}$ and $OSR_{550}$ due to the lack of superficial interaction with the NR/SBR matrix. Reasonably, the lower interaction can be attributed to the higher hydrophobic character of superficial functional groups in the case of the $OSR_{550}$ complex, which is due to the lower degree of graphitization. In virtue of the lower pyrolysis temperature, indeed, the $OSR_{550}$ structure includes a lower graphitic/amorphous C ratio, with a higher presence of superficial carboxylic and hydroxy groups (Figure 2b) that forward a poorer filler−matrix interaction. The pull-out behavior was far more evident in the $SWP_{700}$ composite, in which filler displacement leaves cavities of ≈100 $\mu$m width. Macroscopically, this phenomenon results in poor mechanical stress dissipation, which decreases even further at higher filler inclusion percentages. Although the $OSR_{550}$ gets included into the rubber matrix, the pull-out behavior of smaller particles (≈50 $\mu$m) is still present, affecting the composite reinforcement by disrupting the polymer network and consequently hindering the elastic response of the final material.

$OSR_{550}$ presents bigger cluster of agglomerates as expected by the lower pyrolysis temperature, whereas $OSR_{700}$ and $MSP_{700}$ are characterized by similar particles morphologies, while $SWP_{700}$ displays nonuniform particle size distribution, as also pointed by DLS curves (Figure 2d). $OSR_{700}$ showed optimal dispersion (Figure 5a) throughout the matrix, unlike $MSP_{700}$ which has a major tendency to form agglomerates. In all cases, their agglomeration tendency can be rationalized by simple chemical considerations (Figure 2b,c). Being $SWP_{700}$ poor in oxygen-containing groups, aromatic interactions prevail favoring agglomeration upon dispersion in the matrix. However, $OSR_{500}$ hydrophilicity (high H/C and O/C ratios) obstructs dispersion in favor of agglomeration (Figure 5b). On the contrary, $OSR_{700}$ and $MSP_{700}$ present adequate H/C and O/C ratios for achieving better filler dispersion.

## CONCLUSIONS

In the study presented herein, a systematic investigation into the potential of biochar as a sustainable alternative to



https://doi.org/10.1021/acssuschemeng.5c05447
ACS Sustainable Chem. Eng. 2025, 13, 15421−15434

conventional carbon black (CB) in elastomer composites for tire manufacturing has been provided. CB has been replaced in ratios of 30, 50, and 70 phr with four classes of biochar differentiated on feedstock and pyrolysis conditions. A thorough characterization of biochar structural features, surface chemistry, particle dimension, and thermal resistance has been carried out in order to clarify the reinforcing mechanism for this filler class. We demonstrated that biochar's reinforcing capabilities are primarily ruled by their structural integrity and features, for which porosity and surface chemistry proved to be key in filler−matrix interaction. Additionally, we proved that $SWP_{700}$ and $OSR_{550}$ biochars tested are not suitable for tire applications, as they interfere with the rubber matrix rather than reinforcing it, resulting in the loss of elastic properties. Oilseed rape straw ($OSR_{700}$) biochar exhibited superior compatibility with the rubber matrix, achieving fine dispersion and a more favorable filler−polymer interaction compared to its counterpart treated at lower temperatures ($OSR_{550}$). On the contrary, biochar derived from softwood ($SWP_{700}$) provided poorer reinforcement despite its vast surface area, while miscanthus straw biochar ($MSP_{700}$) caused excessive rubber stiffening in contrast to the relative reinforcement. The emerging divergence was attributed to the different pore size architecture linked to inadequate superficial functional groups.

According to the mechanical and rheological analyses, biochar's reinforcement mechanism deviates from the usual CB model as it is predominantly governed by porosity-mediated polymer entanglement rather than superficial interaction alone. While biochar-filled composites exhibited a reduction in absolute tensile strength compared to $C_0$-CB formulation, $C_1$−$OSR_{700}$ at 50 phr maintained competitive properties in terms of toughness and rolling resistance, demonstrating their viability for tire applications.

Payne effect and dynamic mechanical behavior served as an indication for determining filler dispersion and dumping properties of the resulting materials, which eventually reinforced the hypothesis of a distinctive filler−polymer network. Therefore, our study introduces a new, more comprehensive model for biochar−matrix interactions that goes beyond surface area to include a broader range of parameters, with varying morphological and chemical characteristics. Although not the first to examine oxygen-containing functional groups under different pyrolysis conditions, it is among the first to systematically correlate these characteristics with mechanical properties in the context of rubber reinforcement.

**Outlook.** Biochar inclusion in tire formulation, therefore, presents a viable strategy to mitigate the environmental impact of tire manufacturing, but most of all, this study offers an opportunity to shed light on the reinforcing mechanism. Clarifying structure−property relationships of biochar-filled polymers is pivotal in the development of high-performance composites with reduced carbon footprint.[67] Biochar-reinforced polymers potentially could serve a broader scope in material science and have proven to be applicable in sensoristics,[68] electronics,[69] membranes for wastewater decontamination,[70] and even catalysis;[71] henceforth; understanding their polymer−biochar interaction model also reflects in these fields.

## ■ ASSOCIATED CONTENT

### Supporting Information

The Supporting Information is available free of charge at https://pubs.acs.org/doi/10.1021/acssuschemeng.5c05447.

Complete TGA analysis, Payne effect curves recorded for each composite, DMA curves comparison for CB and $C_1$−$OSR_{700}$ at 30, 50, and 70 phr replacement, as well as FTIR analysis and SEM micrographs of pristine biochar samples, summary tables regarding biochar properties, particle distribution, and rubber composites formulation and their comprehensive mechanical properties (PDF)

## ■ AUTHOR INFORMATION


### Corresponding Author

**C. Noè** − *Department of Applied Science and Technology, Politecnico di Torino, Torino 10129, Italy;* orcid.org/0000-0001-8982-0299; Email: camilla.noe@polito.it

### Authors

**C. Di Bernardo** − *Department of Applied Science and Technology, Politecnico di Torino, Torino 10129, Italy;* orcid.org/0000-0002-1061-9494

**M. Messori** − *Department of Applied Science and Technology, Politecnico di Torino, Torino 10129, Italy*

Complete contact information is available at: https://pubs.acs.org/10.1021/acssuschemeng.5c05447


### Author Contributions

The manuscript was written through contributions of all authors. All authors have given approval to the final version of the manuscript.


### Funding

Agreement for the innovation "X HP NG PEU - NEXT GENERATION Innovative High-Performance Tires, Circular and Sustainable" from Michelin Italy and Ministry Of Enterprises and Made in Italy


### Notes

The authors declare no competing financial interest.

## ■ ACKNOWLEDGMENTS


This work was supported as part of a Michelin S.p.A. project in collaboration with the Department of Applied Science and Technology. The authors acknowledge the use of Department facilities, especially the use of SEM equipment from Prof. Chiara Vitale Brovarone. The authors would also like to acknowledge Prof. Marco Sangermano for the availability of FTIR-ATR machine, Prof. Alberto Frache for the use of Surface Analysis Laboratory in Alessandria facilities, and Prof. Mauro Giorcelli and UK Biochar Research Center for supplying the biochar samples used in this study. Finally, Carlo Amata and Alice Benedetto Mas are thanked for their crucial support during BET and DLS analysis of biochar.


## ■ REFERENCES


(1) Fan, Y.; Fowler, G. D.; Zhao, M. The Past, Present and Future of Carbon Black as a Rubber Reinforcing Filler−A Review. *J. Clean Prod* **2020**, *247*, 119115.

(2) Thomas, J.; Patil, R. The Road to Sustainable Tire Materials: Current State-of-the-Art and Future Prospectives. *Environ. Sci. Technol.* **2023**, *57* (6), 2209−2216.

(3) Phumnok, E.; Khongprom, P.; Ratanawilai, S. Preparation of Natural Rubber Composites with High Silica Contents Using a Wet Mixing Process. *ACS Omega* **2022**, *7* (10), 8364−8376.
(4) Guo, B.; Chen, F.; Lei, Y.; Chen, W. Significantly Improved Performance of Rubber/Silica Composites by Addition of Sorbic Acid. *Polym. J.* **2010**, *42* (4), 319−326.
(5) Kazemi, H.; Mighri, F.; Rodrigue, D. A Review of Rubber Biocomposites Reinforced with Lignocellulosic Fillers. *J. Compos. Sci.* **2022**, *6* (7), 183.
(6) Studebaker, M. L. The Chemistry of Carbon Black and Reinforcement. *Rubber Chem. Technol.* **1957**, *30* (5), 1400−1483.
(7) El-Maadawy, M. M.; Elzoghby, A. A.; Masoud, A. M.; Eldeeb, A. M.; El Naggar, A. M. A.; Taha, M. H. Conversion of Carbon Black Recovered from Waste Tires into Activated Carbon via Chemical/Microwave Methods for Efficient Removal of Heavy Metal Ions from Wastewater. *RSC Adv.* **2024**, *14* (9), 6324−6338.
(8) Choi, S. S. Difference in Bound Rubber Formation of Silica and Carbon Black with Styrene-Butadiene Rubber. *Polym. Adv. Technol.* **2002**, *13* (6), 466−474.
(9) Araujo-Morera, J.; Verdejo, R.; López-Manchado, M. A.; Hernández Santana, M. Sustainable Mobility: The Route of Tires through the Circular Economy Model. *Waste Manage.* **2021**, *126*, 309−322.
(10) Zhang, X.; Li, H.; Cao, Q.; Jin, L.; Wang, F. Upgrading Pyrolytic Residue from Waste Tires to Commercial Carbon Black. *Waste Manag. Res* **2018**, *36* (5), 436−444.
(11) Gao, N.; Wang, F.; Quan, C.; Santamaria, L.; Lopez, G.; Williams, P. T. Tire Pyrolysis Char: Processes, Properties, Upgrading and Applications. *Prog. Energy Combust. Sci.* **2022**, *93*, 101022.
(12) Xu, J.; Yu, J.; Xu, J.; Sun, C.; He, W.; Huang, J.; Li, G. High-Value Utilization of Waste Tires: A Review with Focus on Modified Carbon Black from Pyrolysis. *Sci. Total Environ* **2020**, *742*, 140235.
(13) Greenough, S.; Dumont, M. J.; Prasher, S. The Physicochemical Properties of Biochar and Its Applicability as a Filler in Rubber Composites: A Review. *Mater. Today Commun.* **2021**, *29*, 102912.
(14) Rajan, K. P.; Gopanna, A.; Theravalappil, R.; Abdelghani, E. A. M.; Thomas, S. P. Partial Replacement of Carbon Black with Graphene in Natural Rubber/Butadiene Rubber Based Tire Compound: Investigation of Critical Properties. *J. Polym. Res.* **2022**, *29* (3), 76.
(15) Malas, A.; Pal, P.; Das, C. K. Effect of Expanded Graphite and Modified Graphite Flakes on the Physical and Thermo-Mechanical Properties of Styrene Butadiene Rubber/Polybutadiene Rubber (SBR/BR) Blends. *Mater. Des.* **2014**, *55*, 664−673.
(16) Mao, Y.; Wen, S.; Chen, Y.; Zhang, F.; Panine, P.; Chan, T. W.; Zhang, L.; Liang, Y.; Liu, L. High Performance Graphene Oxide Based Rubber Composites. *Sci. Rep* **2013**, *3* (1), 1−7.
(17) Sui, G.; Zhong, W. H.; Yang, X. P.; Yu, Y. H.; Zhao, S. H. Preparation and Properties of Natural Rubber Composites Reinforced with Pretreated Carbon Nanotubes. *Polym. Adv. Technol.* **2008**, *19* (11), 1543−1549.
(18) Capecchi, E.; Tomaino, E.; Piccinino, D.; Kidibule, P. E.; Fernández-Lobato, M.; Spinelli, D.; Pogni, R.; Cabado, A. G.; Lago, J.; Saladino, R. Nanoparticles of Lignins and Saccharides from Fishery Wastes as Sustainable UV-Shielding, Antioxidant, and Antimicrobial Biofillers. *Biomacromolecules* **2022**, *23* (8), 3154−3164.
(19) Miedzianowska, J.; Masłowski, M.; Rybinski, P.; Strzelec, K. Properties of Chemically Modified (Selected Silanes) Lignocellulosic Filler and Its Application in Natural Rubber Biocomposites. *Materials* **2020**, *13* (18), 4163.
(20) Hou, Y.; Wu, W. Derived from Corn Straw Cellulose: Modified Used Tire Rubber Powder Composites. *Cellulose* **2022**, *29* (7), 3935−3945.
(21) Mohit, H.; Arul Mozhi Selvan, V. A Comprehensive Review on Surface Modification, Structure Interface and Bonding Mechanism of Plant Cellulose Fiber Reinforced Polymer Based Composites. *Compos Interfaces* **2018**, *25* (5−7), 629−667.
(22) Hornig, S.; Heinze, T. Efficient Approach to Design Stable Water-Dispersible Nanoparticles of Hydrophobic Cellulose Esters. *Biomacromolecules* **2008**, *9* (5), 1487−1492.
(23) Heinze, T.; Liebert, T. Unconventional Methods in Cellulose Functionalization. *Prog. Polym. Sci.* **2001**, *26* (9), 1689−1762.
(24) Hu, J.; Kong, Z.; Liu, K.; Qin, J.; Tao, Y.; Zhou, L.; Yuan, Y.; Jiang, M.; Duan, Y.; Zhang, J. Carboxylation of Cellulose Nanocrystals for Reinforcing and Toughing Rubber through Dual Cross-Linking Networks. *ACS Appl. Polym. Mater.* **2021**, *3* (12), 6120−6129.
(25) Roy, K.; Pongwisuthiruchte, A.; Chandra Debnath, S.; Potiyaraj, P. Application of Cellulose as Green Filler for the Development of Sustainable Rubber Technology. *Curr. Res. Green Sustain. Chem* **2021**, *4*, 100140.
(26) Chen, W. J.; Gu, J.; Xu, S. H. Exploring Nanocrystalline Cellulose as a Green Alternative of Carbon Black in Natural Rubber/Butadiene Rubber/Styrene-Butadiene Rubber Blends. *Express Polym. Lett.* **2014**, *8* (9), 659−668.
(27) Okita, Y.; Fujisawa, S.; Saito, T.; Isogai, A. TEMPO-Oxidized Cellulose Nanofibrils Dispersed in Organic Solvents. *Biomacromolecules* **2011**, *12* (2), 518−522.
(28) Yuan, H.; Nishiyama, Y.; Wada, M.; Kuga, S. Surface Acylation of Cellulose Whiskers by Drying Aqueous Emulsion. *Biomacromolecules* **2006**, *7* (3), 696−700.
(29) Somseemee, O.; Sae-Oui, P.; Siriwong, C. Reinforcement of Surface-Modified Cellulose Nanofibrils Extracted from Napier Grass Stem in Natural Rubber Composites. *Ind. Crops Prod.* **2021**, *171*, 113881.
(30) Choudhary, M.; Singh, D.; Devnani, G. L.; Mishra, A. Impact of Various Surface Modifications on Agro Waste Rice Husk and Its Reinforced Polymer Composites. *Mater. Today Proc.* **2021**, *45*, 4760−4762.
(31) Barkane, A.; Kampe, E.; Gaidukovs, S. New Reinforcing Approach for Biobased UV-Curing Resins: Hybrid Lignocellulose Fillers with Improved Synergy and Wood Structure Mimics. *ACS Sustainable Chem. Eng* **2023**, *11*, 6578−6591.
(32) Dominic, M.; Joseph, R.; Sabura Begum, P. M.; Kanoth, B. P.; Chandra, J.; Thomas, S. Green Tire Technology: Effect of Rice Husk Derived Nanocellulose (RHNC) in Replacing Carbon Black (CB) in Natural Rubber (NR) Compounding. *Carbohydr. Polym.* **2020**, *230*, 115620.
(33) Thomas, S. K.; Begum, P. M. S.; Dileep, P.; Neenu, K. V.; David, D. A.; Santu, A.; Midhun Dominic, C. D. Composites of Resorcinol and Hexamethylenetetramine Modified Nanocellulose Whiskers as Potential Biofiller in Natural Rubber Latex: Synthesis, Characterization and Property Evaluation. *Biomass Convers Biorefin* **2023**, *14*, 16769−16785.
(34) Aboughaly, M.; Babaei-Ghazvini, A.; Dhar, P.; Patel, R.; Acharya, B. Enhancing the Potential of Polymer Composites Using Biochar as a Filler: A Review. *Polymers* **2023**, *15* (19), 3981.
(35) Kim, P.; Johnson, A.; Edmunds, C. W.; Radosevich, M.; Vogt, F.; Rials, T. G.; Labbé, N. Surface Functionality and Carbon Structures in Lignocellulosic-Derived Biochars Produced by Fast Pyrolysis. *Energy Fuels* **2011**, *25* (10), 4693−4703.
(36) Xiao, X.; Chen, Z.; Chen, B. H/C Atomic Ratio as a Smart Linkage between Pyrolytic Temperatures, Aromatic Clusters and Sorption Properties of Biochars Derived from Diverse Precursory Materials. *Sci. Rep.* **2016**, *6* (1), 2016.
(37) Bélanger, N.; Macek, H.; Gariépy, Y.; Francis, M.; Prasher, S.; Khripin, C. Y.; Mehlem, J. J.; Dumont, M. J. Evaluating Corn-Based Biochar as an Alternative to Carbon Black in Styrene-Butadiene Rubber Composites. *Mater. Today Commun.* **2023**, *34*, 105218.
(38) Bélanger, N.; Prasher, S.; Dumont, M.-J. Tailoring Biochar Production for Use as a Reinforcing Bio-Based Filler in Rubber Composites: A Review. *Polym. Plast. Technol. Mater* **2023**, *62* (1), 54−75.
(39) Kaliyathan, A. V.; Rane, A. V.; Huskic, M.; Kunaver, M.; Kalarikkal, N.; Rouxel, D.; Thomas, S. Carbon Black Distribution in Natural Rubber/Butadiene Rubber Blend Composites: Distribution Driven by Morphology. *Compos. Sci. Technol.* **2020**, *200*, 108484.

(40) El-Hendawy, A. N. A.; Alexander, A. J.; Andrews, R. J.; Forrest, G. Effects of Activation Schemes on Porous, Surface and Thermal Properties of Activated Carbons Prepared from Cotton Stalks. *J. Anal. Appl. Pyrolysis* **2008**, *82* (2), 272−278.
(41) Khonakdar, H. A.; Morshedian, J.; Wagenknecht, U.; Jafari, S. H. An Investigation of Chemical Crosslinking Effect on Properties of High-Density Polyethylene. *Polymer (Guildf)* **2003**, *44* (15), 4301−4309.
(42) Menczel, J. D.. In *Thermal Analysis of Polymers:Fundamentals and Applications*; Menczel, J. D., Prime, R. B., Eds.; Wiley, 2009.
(43) Schoff, C. K. Dynamic Mechanical Analysis. *CoatingsTech* **2008**, *5* (10), 44.
(44) Szymanski, H. A. Alkenes. *Interpret. Infrared Spectra* **1964**, 31−77.
(45) Pasquali, C. E. L.; Herrera, H. Pyrolysis of Lignin and IR Analysis of Residues. *Thermochim. Acta* **1997**, *293* (1−2), 39−46.
(46) Janu, R.; Mrlik, V.; Ribitsch, D.; Hofman, J.; Sedláček, P.; Bielská, L.; Soja, G. Biochar Surface Functional Groups as Affected by Biomass Feedstock, Biochar Composition and Pyrolysis Temperature. *Carbon Resour. Convers.* **2021**, *4*, 36−46.
(47) Hoshikawa, Y.; An, B.; Kashihara, S.; Ishii, T.; Ando, M.; Fujisawa, S.; Hayakawa, K.; Hamatani, S.; Yamada, H.; Kyotani, T. Analysis of the Interaction between Rubber Polymer and Carbon Black Surfaces by Efficient Removal of Physisorbed Polymer from Carbon-Rubber Composites. *Carbon N Y* **2016**, *99*, 148−156.
(48) Valentín, J. L.; Mora-Barrantes, I.; Carretero-González, J.; López-Manchado, M. A.; Sotta, P.; Long, D. R.; Saalwächter, K. Novel Experimental Approach to Evaluate Filler-Elastomer Interactions. *Macromolecules* **2010**, *43* (1), 334−346.
(49) Shi, X.; Sun, S.; Zhao, A.; Zhang, H.; Zuo, M.; Song, Y.; Zheng, Q. Influence of Carbon Black on the Payne Effect of Filled Natural Rubber Compounds. *Compos. Sci. Technol.* **2021**, *203*, 108586.
(50) Ramier, J.; Gauthier, C.; Chazeau, L.; Stelandre, L.; Guy, L. Payne Effect in Silica-Filled Styrene−Butadiene Rubber: Influence of Surface Treatment. *J. Polym. Sci. B Polym. Phys.* **2007**, *45* (3), 286−298.
(51) Gan, S.; Wu, Z. L.; Xu, H.; Song, Y.; Zheng, Q. Viscoelastic Behaviors of Carbon Black Gel Extracted from Highly Filled Natural Rubber Compounds: Insights into the Payne Effect. *Macromolecules* **2016**, *49*, 1454−1463.
(52) Wang, Y.; Maurel, G.; Couty, M.; Detcheverry, F.; Merabia, S. Microscopic Interpretation of the Payne Effect in Model Fractal Aggregate Polymer Nanocomposites. *Macromolecules* **2024**, *57* (8), 3636−3646.
(53) Kawak, P.; Bhapkar, H.; Simmons, D. S. Central Role of Filler−Polymer Interplay in Nonlinear Reinforcement of Elastomeric Nanocomposites. *Macromolecules* **2024**, *57* (19), 9466−9475.
(54) Davris, T.; Mermet-Guyennet, M. R. B.; Bonn, D.; Lyulin, A. V. Filler Size Effects on Reinforcement in Elastomer-Based Nanocomposites: Experimental and Simulational Insights into Physical Mechanisms. *Macromolecules* **2016**, *49*, 7077−7087.
(55) Huang, L.; Yu, F.; Liu, Y.; Lu, A.; Song, Z.; Liu, W.; Xiong, Y.; He, H.; Li, S.; Zhao, X.; Cui, S.; Zhu, C. Understanding the Reinforcement Effect of Fumed Silica on Silicone Rubber: Bound Rubber and Its Entanglement Network. *Macromolecules* **2023**, *56* (1), 323−334.
(56) Mullins, L. Softening of Rubber by Deformation. *Rubber Chem. Technol.* **1969**, *42* (1), 339−362.
(57) Liang, X.; Nakajima, K. Study of the Mullins Effect in Carbon Black-Filled Styrene−Butadiene Rubber by Atomic Force Microscopy Nanomechanics. *Macromolecules* **2022**, *55*, 6023−6030.
(58) Bokobza, L. Elastomer Nanocomposites: Effect of Filler−Matrix and Filler−Filler Interactions. *Polymers* **2023**, *15* (13), 2900.
(59) Ritchie, R. O. The Conflicts between Strength and Toughness. *Nat. Mater.* **2011**, *10* (11), 817−822.
(60) Liao, X.; Dulle, M.; De Souza E Silva, J. M.; Wehrspohn, R. B.; Agarwal, S.; Förster, S.; Hou, H.; Smith, P.; Greiner, A. High Strength in Combination with High Toughness in Robust and Sustainable Polymeric Materials. *Science* **2019**, *366* (6471), 1376−1379.
(61) Fang, Z.; Mu, H.; Sun, Z.; Zhang, K.; Zhang, A.; Chen, J.; Zheng, N.; Zhao, Q.; Yang, X.; Liu, F.; Wu, J.; Xie, T. 3D Printable Elastomers with Exceptional Strength and Toughness. *Nature* **2024**, *631*, 783−788.
(62) Fan, J.; Zhou, Y.; Ding, S.; Pang, Y.; Zeng, X.; Guo, S.; Xu, J.; Ren, L.; Sun, R.; Zeng, X. Thermally Conductive Elastomer Composites with High Toughness, Softness, and Resilience Enabled by Regulating Interfacial Structure and Dynamics. *Small* **2024**, *20* (38), 2402265.
(63) Ferry, J. D. *Viscoelastic Properties of Polymers*; Wiley, 1980, PDF | PDF. https://www.scribd.com/document/458215908/John-D-ferry-Viscoelastic-Properties-of-Polymers-Wiley-1980-pdf (accessed 2025−02−18).
(64) Bijina, V.; Jandas, P. J.; Jose, J.; Muhammed Ajnas, N.; Abhitha, K. P.; John, H. Tuning the Low Rolling Resistance, Wet Grip, and Heat Build-up Properties of Tyre Tread Formulations Using Carbon Black/Thermally Exfoliated Graphite Hybrid Fillers. *J. Appl. Polym. Sci.* **2022**, *140*, No. e53508.
(65) Li, M.; Zhu, L.; Xiao, H.; Shen, T.; Tan, Z.; Zhuang, W.; Xi, Y.; Ji, X.; Zhu, C.; Ying, H. Design of a Lignin-Based Versatile Bioreinforcement for High-Performance Natural Rubber Composites. *ACS Sustain. Chem. Eng.* **2022**, *10* (24), 8031−8042.
(66) Shorey, R.; Gupta, A.; Mekonnen, T. H. Hydrophobic Modification of Lignin for Rubber Composites. *Ind. Crops Prod.* **2021**, *174*, 114189.
(67) Tengku Yasim-Anuar, T. A.; Yee-Foong, L. N.; Lawal, A. A.; Ahmad Farid, M. A.; Mohd Yusuf, M. Z.; Hassan, M. A.; Ariffin, H. Emerging Application of Biochar as a Renewable and Superior Filler in Polymer Composites. *RSC Adv.* **2022**, *12* (22), 13938−13949.
(68) Cao, L.; Ding, Q.; Liu, M.; Lin, H.; Yang, D. P. Biochar-Supported Cu2+/Cu+Composite as an Electrochemical Ultrasensitive Interface for Ractopamine Detection. *ACS Appl. Bio Mater.* **2021**, *4* (2), 1424−1431.
(69) Natalio, F.; Corrales, T. P.; Feldman, Y.; Lew, B.; Graber, E. R. Sustainable Lightweight Biochar-Based Composites with Electromagnetic Shielding Properties. *ACS Omega* **2020**, *5* (50), 32490−32497.
(70) Tan, X.-f.; Liu, Y.-g.; Gu, Y.-l.; Xu, Y.; Zeng, G.-m.; Hu, X.-; Liu, S.-b.; Wang, X.; Liu, S.-m.; Li, J. Biochar-Based Nano-Composites for the Decontamination of Wastewater: A Review. *Bioresour. Technol.* **2016**, *212*, 318−333.
(71) Lyu, H.; Zhang, Q.; Shen, B. Application of Biochar and Its Composites in Catalysis. *Chemosphere* **2020**, *240*, 124842.